

Non-invasive monitoring of cardiac contractility and sympathetic drive: Trans-Radial Electrical Bioimpedance Velocimetry (TREV)

Alexandra Stump¹, Caitlin Gregory¹, Viktoriya Babenko¹, Elizabeth Rizor¹, Tom Bullock¹, Alan Macy², Barry Giesbrecht¹, Scott Grafton¹, and Neil M. Dundon¹

¹University of California Santa Barbara

²Biopac Systems, Inc.

March 27, 2023

Abstract

We describe methods and software resources for a bioimpedance measurement technique, “trans-radial electrical bioimpedance velocimetry” that allows for the non-invasive monitoring of relative cardiac contractility and stroke volume, proxies of sympathetic cardiac tone. In addition to describing the general recording methodology, which requires impedance measurements of the forearm, we provide open source Jupyter based software (operable on most computers) for deriving cardiac contractility from the impedance measurements. We demonstrate the ability of this bioimpedance measurement for tracking event related contractility in a maximal grip force production task. Critically, the results demonstrate both a reactive increase in cardiosympathetic drive with force production as well as a learned increase in drive prior to grip onset, consistent with allostatic autonomic regulation. The method and software should be of broad utility for investigations of event related cardio-sympathetic regulation in psychophysical studies.

1 Non-invasive monitoring of cardiac contractility and sympathetic drive: Trans-Radial Electrical
2 Bioimpedance Velocimetry (TREV)

3
4 Alexandra Stump^{1*}

5 Caitlin Gregory^{1*}

6 Viktoriya Babenko¹

7 Elizabeth Rizer¹

8 Tom Bullock^{1,2}

9 Alan Macy³

10 Barry Giesbrecht^{1,2}

11 Scott T Grafton^{1,2}

12 Neil M Dundon^{1,2,3}

13 *Contributed equally as first author

14
15 ¹Department of Psychological and Brain Sciences, University of California, Santa Barbara, CA 93106, USA

16 ²Institute for Collaborative Biotechnologies, University of California, Santa Barbara, CA 93106, USA

17 ³Department of Child and Adolescent Psychiatry, Psychotherapy and Psychosomatics, University of
18 Freiburg, 79104 Freiburg, Germany

19 ⁴BIOPAC Systems, Inc, Goleta, CA, USA.

20

21 Corresponding Author: neil.dundon@psych.ucsb.edu

22

23

24

25 Abstract

26 We describe methods and software resources for a bioimpedance measurement technique, “trans-radial
27 electrical bioimpedance velocimetry” that allows for the non-invasive monitoring of relative cardiac
28 contractility and stroke volume, proxies of sympathetic cardiac tone. In addition to describing the
29 general recording methodology, which requires impedance measurements of the forearm, we provide
30 open source Jupyter based software (operable on most computers) for deriving cardiac contractility from
31 the impedance measurements. We demonstrate the ability of this bioimpedance measurement for
32 tracking event related contractility in a maximal grip force production task. Critically, the results
33 demonstrate both a reactive increase in cardiosympathetic drive with force production as well as a
34 learned increase in drive prior to grip onset, consistent with allostatic autonomic regulation. The method
35 and software should be of broad utility for investigations of event related cardio-sympathetic regulation
36 in psychophysical studies.

37

38 Introduction

39 The cardiovascular system adapts quickly and dynamically in anticipation of and in response to a
40 variety of stressors. Tracking these perturbations of sympathetic control by a measurement with high
41 temporal resolution is a promising approach for identifying both physiological and psychological drivers
42 of stress (Cieslak, et al., 2018). Bioimpedance methods, particularly impedance cardiography (ICG), have
43 long been used to investigate the sympathetic branch of the autonomic nervous system to the heart by
44 capturing electromechanical modulation of cardiovascular activity during cognitive tasks (Miller &
45 Horvath, 1978). ICG uses a high frequency electrical current delivered via a total of 8 pairs of electrodes
46 placed on the neck and thorax, while another pair of electrodes are required to record the
47 electrocardiogram. Using the combination of impedance cardiography and electrocardiography, a
48 number of cardiodynamic parameters that are sensitive to sympathetic drive can be derived. These
49 include intervallic parameters such as left ventricular ejection time (LVET) and pre-ejection period (PEP)
50 as well as estimates of stroke volume (SV) and cardiac output (CO) based on idealized models of the
51 thorax (Bernstein, 2009).

52 While ICG is a powerful approach, the method has drawbacks. Because the measurements are
53 acquired across the thorax, the normal respiratory cycle introduces a complex set of confounds including
54 changes of thoracic size and shape that undermine the application of ideal models. Furthermore, cyclic
55 changes of intrathoracic pressure and venous return to the heart introduce added uncertainty in isolating
56 sympathetic dynamics from other physiologic control variables. Pragmatically, motion artifacts and
57 operational challenges related to applying electrodes to the naked torso pose additional limitations.
58 More problematic has been the modeling of the resultant thoracic impedance waveform. The analysis
59 depends on the identification of the b-point, a subtle inflection of the impedance wave corresponding to
60 the opening of the aortic valve. Despite the development and distribution of semi-automated software
61 tools by our lab for expediting the labeling of the b-point, we find that for many studies b-point

62 identification continues to require extensive hands-on expert quality control for labeling ambiguous time
63 points. While the variability in labeling the b-point can be overcome by averaging heart beats over a
64 sliding time window, this compromises the goal of measuring sympathetic responses on a fast time scale
65 (Cieslak, et al., 2018).

66 Given the ongoing challenges of ICG analysis and the goal of characterizing cardiosympathetic
67 drive on a beat-by-beat time scale, we have investigated other bioimpedance measurements besides
68 ICG (Sel, Osman, & Jafari, 2021). Here we present a particularly promising method called Trans-Radial
69 Electrical Bioimpedance Velocimetry (TREV) (Bernstein, Henry, Banet, & Dittrich, 2012). In contrast to
70 ICG, TREV is a user-friendly approach that avoids many of the problems that result from acquiring signals
71 across the thorax. Instead, impedance signals with TREV are measured across the length of the volar
72 forearm. Changes of the impedance signal are directly related to a pressure wave propagating along the
73 radial and ulnar arteries that arises with the opening of the aortic valve. In the following sections, we
74 describe the underlying biomechanical and electrical properties of TREV that lead to the estimation of
75 cardiac contractility. We demonstrate the utility of this approach with an isometric grip force task to
76 capitalize on the known increase in sympathetic activation while humans apply their maximum grip force
77 to a grip transducer (Richter, 2015; Richter, Gendolla, & Wright, 2016; Stanek & Richter, 2016; Stanek &
78 Richter, 2021). We show that TREV is capable of capturing beat by beat allostatic anticipatory changes of
79 the sympathetic nervous system, suggesting that participants can learn to develop a sympathetic
80 response prior to movement onset. Finally, we provide signal processing software operable on most
81 computers and a tutorial for streamlining the conversion of TREV impedance measurements into beat-
82 by-beat estimates of contractility.

83

84 I. Background Physics and Physiology

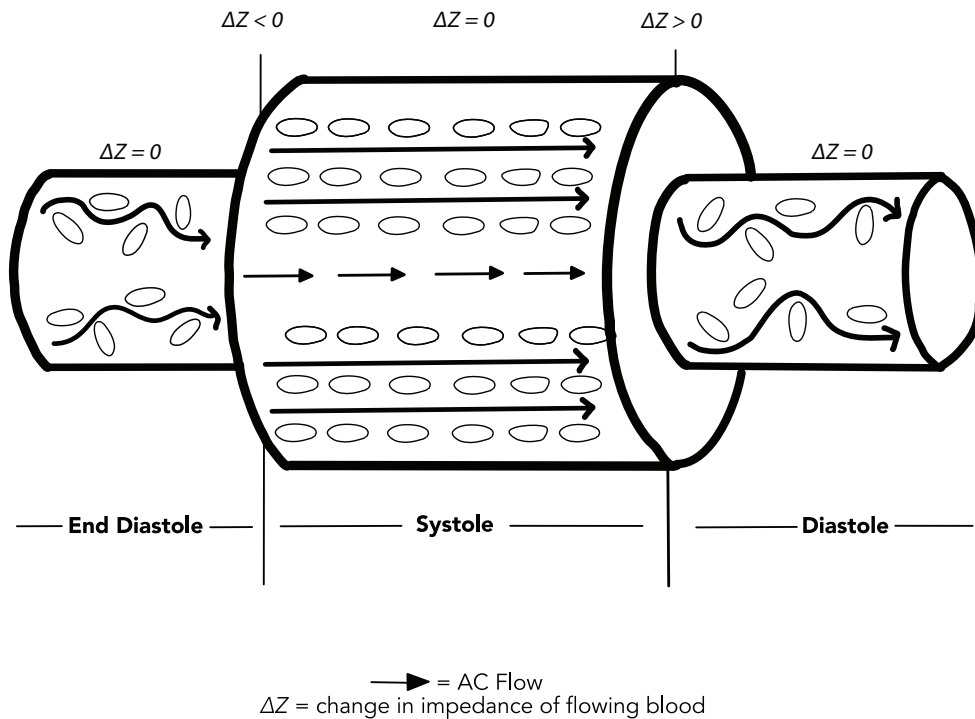
85 *Red blood cells and impedance*

86 Several biophysical properties contribute to the changes of electrical impedance measured with
87 TREV. Under static conditions (without blood flow or arterial pressure gradients), the red blood cells,
88 constituting approximately 40% of blood volume in a vessel, will be randomly oriented. Due to the
89 random orientation of the biconcave red blood cells, an increased resistance within the plasma is
90 observed, as the artery exhibits a maximal level of electrical resistivity (Bernstein, 2009). During normal
91 blood flow through the radial and ulnar arteries, the short axis of red blood cells aligns perpendicular to
92 the flow axis. Additionally, impedance Z (measured in ohms/sec) and blood volume will vary as a
93 function of velocity (v), which we assume remains constant along the measured segments of the two
94 arteries. It is important to note that the denotation of Z in ohms per second is a departure from the
95 typical usage of Z in other branches of physics where Z is expressed in units of ohms (Bernstein, Henry,
96 Banet, & Dittrich, 2012).

97

98

99



100

101 Figure 1: Pulsatile blood flow through the artery of the forearm. During systole, the pressure wave both dilates the
 102 blood vessel and rapidly aligns red blood cells, resulting in decreased impedance. Adapted from (Bernstein, 2009).

103

104 *Generation of a pressure wave*

105 During diastole of the cardiac cycle, the aortic valve is closed, isolating aortic blood pressure
 106 from intraventricular pressure as blood fills the ventricle, boosted by atrial contraction. With systole, the
 107 ventricular myocardium contracts, the mitral valve closes and isovolumic intraventricular pressure rapidly
 108 rises until pressure in the ventricle surpasses aortic pressure, at which point the aortic valve opens. A
 109 pressure surge occurs at this moment. This near instantaneous pressure wave is rapidly transmitted
 110 throughout the arterial vasculature. In a stiff pipe, this wave travels at a velocity of 1280 m/s. Because the
 111 vasculature, particularly the proximal aorta, is compliant, there is both a delay and dispersion of this
 112 pressure wave compared to a rigid pipe. With TREV, when this slightly delayed and dampened pressure
 113 wave arrives in the arteries of the forearm the red blood cells will further align as shown in Figure 1. The

114 net effect is a decrease in impedance Z . As shown in Figure 1 there can also be an increase in blood
115 volume; however, changes in blood volume in the forearm vasculature are relatively minor.

116 Cardiac contractility, or the vigor with which the heart contracts, will determine in large part the
117 intraventricular pressure that is generated during systole. As sympathetic activity increases, cardiac
118 contractility also increases. Thus, contractility is a particularly useful variable of interest for tracking
119 sympathetic dynamics in psychophysiological research. For a healthy individual at rest, end-diastolic
120 ventricular volume will also impact intraventricular pressure and potentially influence the pressure wave
121 and stroke velocity that change impedance. Critically, the greater the ventricular contractility, the higher
122 the stroke velocity and change of impedance. To better characterize this change, we can take the
123 derivative of stroke velocity which we can refer to as acceleration, measured as dZ/dt in units of ohms
124 per second squared. In a single cardiac cycle, the maximum of the acceleration wave corresponds to the
125 time at which the radial artery has the lowest resistivity. We can take the derivative of acceleration (in
126 engineering, this is known as 'jerk'), to obtain contractility, (d^2Z/dt^2), in ohms per second cubed. This
127 wave can be interpreted as the strength at which the acceleration is generated, which occurs at the
128 moment the aortic valve opens, and reflects the maximal isovolumic ventricular pressure. In addition to
129 contractility, stroke volume can also be calculated by integrating the normalized acceleration curve. A
130 previous validation study demonstrates good correlation between cardiac MRI and TREV based
131 estimates of stroke volume and cardiac output (Bernstein, et al., 2015)

132 The key benefit of TREV over ICG is that with the former, the measure is based on blood flow
133 through the linear axially-oriented segments of the radial (and ulnar) artery as opposed to multi-oriented
134 flow directions in the heart, aortic arch and heavily branching thoracic vasculature. The linear,
135 longitudinal orientation of the radial and ulnar arteries in the forearm simplifies the relationship between
136 impedance, blood flow and stroke velocity generated by the vigor of cardiac contractility. A similar
137 relationship is not obtainable with ICG because the thoracic impedance measurement cannot distinguish

138 pressure-induced impedance changes in the aorta from those occurring in the ventricle, as both are
139 within the field of measurement. Because of the limitations of impedance cardiography alone, the
140 combination of ICG and EKG must be performed to derive measurements of sympathetic: PEP, LVET,
141 SV, and CO. Thus, TREV's advantageous design comes from the ability to derive a direct measurement
142 of sympathetic activation, contractility, without the usage of a 10-electrode ICG-EKG system. Additional
143 information on the mathematical derivation of contractility, effect of compliance, and extension to
144 estimations of stroke volume are available as a supplement that accompanies the Jupyter software
145 described below.

146

147 II. Anticipatory changes of cardiac contractility with isometric force production

148 In this section we demonstrate changes in contractility associated with the isometric force
149 produced by bilateral maximum strength hand grips. Using repeated measures of grips, it is possible to
150 observe the development of an anticipatory change in contractility prior to grip onset, consistent with
151 allostatic regulation by the autonomic nervous system (McEwen & Wingfield, 2003).

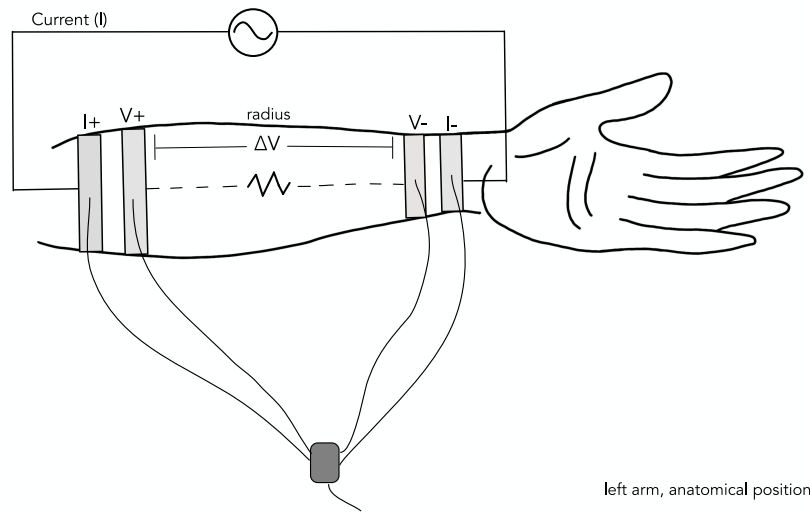
152 Materials and Methods

153 *Participants and experimental overview*

154 Thirty-one healthy humans (19 females) participated in the study after providing informed
155 consent in accordance with the University of California, Santa Barbara (UCSB) Institutional Review Board.
156 Participants self-reported no cardiovascular abnormalities. The average age of participants was 23.4
157 years. One participant was excluded due to excessively noisy data, leaving a final sample of $n = 30$.
158 Participants were compensated \$10/hour plus a potential \$10 bonus depending on task performance
159 (see Grip Task below).

160 Participants performed two blocks of a maximum grip task (Grip Task), each block corresponding
161 to three sequential grips of one hand and then the other (with hand order randomized across subjects).

162 Three simultaneous physiological timeseries were recorded in each block. The first timeseries was time-
 163 varying cardiac impedance derived from TREV, with electrodes attached to the forearm contralateral to
 164 the hand administering grips (Figure 2). The second timeseries was a standard electrocardiogram (EKG).
 165 The last timeseries recorded the continuous respiration cycle with an abdominal belt.



166
 167 Figure 2: Electrode placement of trans-radial electrical bioimpedance velocimetry system. Four electrodes placed on
 168 the forearm; two outer current electrodes (I+ and I-) and two inner voltage sensing electrodes (V+ and V-). I+ and I-
 169 create an alternating current field (I) through the forearm, and any changes in forearm impedance are directly
 170 correlated to changes in voltage ΔV between V+ and V-.

171
 172 *Recording Apparatus*

173 TREV electrodes were amplified by an NICO100D (BIOPAC Systems, Inc., Goleta, CA, USA)
 174 smart amplifier. A current field is applied across the forearm by means of a constant magnitude, high
 175 frequency (50-100 kHz) low amplitude alternating current (4 mA RMS). The constant current (I) is
 176 introduced through the two outer electrodes (I+ and I-) and the resulting voltage (V) is measured via the
 177 inner electrodes (V+ and V-). Using Ohm's Law, we can use the voltage differential V and applied current I
 178 to calculate impedance Z (measured in ohms):

179
$$Z(t) = V(t) / I(t)$$

180 Here, I and V are the root mean square values of the known current and measured voltage.
181 Because the magnitude of the current I is constant, any change in voltage V over time will vary in direct
182 proportion to changes in impedance Z . This method allows us to capture moment-to-moment
183 fluctuations in bioimpedance, which directly correlate with perturbations in the autonomic nervous
184 system.

185 Electrocardiogram electrodes were amplified by an ECG100D (BIOPAC Systems, Inc.) smart
186 amplifier. Respiration cycle was recorded using a TSD221-MRI (BIOPAC Systems, Inc.) respiration belt.
187 Force exerted in the Grip Task was recorded using an SS56L (BIOPAC Systems, Inc.) grip bulb. All
188 continuous signals were integrated using an MP160 (BIOPAC Systems, Inc.) amplifier and processed
189 online using BIOPAC AcqKnowledge software (BIOPAC Systems, Inc.). Visual stimuli were presented on
190 a 21" monitor using Microsoft PowerPoint. Offline preprocessing of recorded timeseries was conducted
191 using the Moving Ensemble Analysis Pipeline (MEAP) and MATLAB (Cieslak, et al., 2018). Bayes models
192 were fitted using No U-Turn sampling (NUTS) Hamiltonian Monte Carlo, fitted with PyMC3 Python3
193 functions (Salvatier, Wiecki, & Fonnesbeck, 2016).

194 *General Procedure*

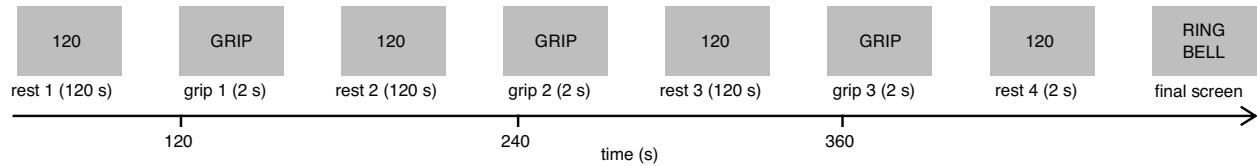
195 All data were recorded in a single session lasting approximately 45 minutes (including initial
196 equipment setup). Participants first washed their hands and forearms with water and regular soap to
197 remove dirt or oily residues. In a private setup room, an experimenter then placed four TREV electrodes
198 on the forearm contralateral to the grip hand of the first block (see Grip Task, below). Two electrodes
199 were placed ventrally on the distal region of the forearm, just below where the wrist meets the hand, and
200 two electrodes on the proximal region of the forearm, just below where the elbow meets the forearm
201 (Figure 2). Each electrode pair was spaced one centimeter apart. TREV electrodes are bioimpedance
202 strip electrodes (BIOPAC EL526 - size 1.3cm x 16.5cm). These electrodes establish circumferential
203 equipotential lines at the four electrode locations.

204 Next, the experimenter placed two EKG electrodes on the participant's chest: one below the
205 right collarbone and one where the deltoid meets the chest. Participants were then brought to the
206 testing room, electrodes were connected to the associated amplifiers, a respiration belt was placed
207 around the participant's abdomen, and they were seated at the testing table 3 feet from a computer
208 screen. Once seated, participants were taught how to properly hold and squeeze the grip bulb, with the
209 tubing facing down and in a manner that involved the whole hand. Participants were also instructed to
210 maintain the same posture and to keep their arms relaxed, still, and in the same positioning on the table
211 throughout the entirety of the experiment.

212 *Grip Task*

213 The experimenter first asked participants to grip the bulb as hard as possible with each hand,
214 recording each maximal value (max thresholds). Participants then performed two blocks of three trials,
215 gripping with the opposite hand in each block (block-hand order was determined with uniform ($p=0.50$)
216 probability for each participant). After recording participants' maximum forces (max thresholds; above),
217 the experimenter then explained the experimental protocol, which is depicted in Figure 3. Prior to the
218 start of the first block of trials, participants were instructed to sit idly for three minutes to acclimate to the
219 exam room. The experimenter then quietly entered the room to start the physiological recording and
220 associated computer task. Once the experiment started, the experimenter departed the room. Trials
221 began with an on-screen countdown timer, where participants were instructed to look at the screen
222 through a two-minute rest period. At the end of the rest period, a "go" cue would appear, signaling to
223 the participants to squeeze the bulb maximally for two seconds. The countdown period of the next trial's
224 rest period then immediately began. This cycle continued for two more grips. At the end of the third trial
225 on each block, a timer counted down to a visual stimulus that instructed participants to ring a bell to
226 alert the experimenter they had finished. Each of the three trials was therefore preceded and followed
227 by a two-minute rest. To incentivize participants to grip with maximum strength, we imposed a bonus

228 system, whereby participants who reached a threshold of $\pm 0.04 \text{ Kg/m}^2$ of their hand-specific max-
229 thresholds on all three grips would win a \$10 bonus. The experimenter disclosed this rule to participants
230 after recording the max thresholds and did not inform participants if they had achieved the bonus until
231 after all testing was completed. After completing the first block, the experimenter transferred the TREV
232 electrodes to the other arm and the grip task was repeated.



234 Figure 3. Within block timing of grip task and rest. This structure was performed for each hand.

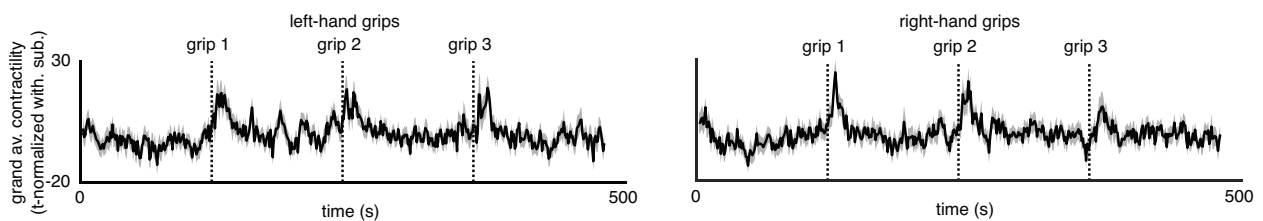
235

236 *Cardiovascular preprocessing*

237 During recording, the AcqKnowledge software was used to apply an online lowpass filter (max
238 cutoff = 20 Hz) to the raw impedance timeseries $Z(t)$ recorded by the TREV electrodes and then
239 calculated as a continuous estimation of acceleration. This raw contractility timeseries was then imported
240 together with the raw EKG and respiration timeseries to the MEAP software for minimal offline
241 processing. MEAP first automatically labelled the R-peaks of the EKG timeseries, which we used as an
242 index for the moment in time to define each individual heartbeat. We next used these R-peak time
243 indices to extract epochs spanning ± 350 ms around each heartbeat from the raw contractility
244 timeseries (contractility epochs). MEAP also computed estimates of heart-rate at each beat from the R-
245 peaks. MEAP outputs were then transferred to MATLAB, where the maximum amplitude in each
246 contractility epoch was computed as an estimation of each heartbeat's contractility (beat-wise
247 contractility timeseries). Then, separately for each subject, and each block, we conducted an additional
248 regression procedure (Dundon, et al., 2020; Dundon, Shapiro, Babenko, Okafor, & Grafton, 2021) to
249 remove the additional confounding effects of heart-rate and respiration from the beat-wise contractility

250 timeseries. Using a multiple regression model, we regressed the vector beat-wise contractility as a
 251 function of an intercept and three regressors: (i) the phase of respiration at each heartbeat, (ii) the
 252 amplitude of respiration at each heartbeat and (iii) the heartrate at each heartbeat. To down sample each
 253 regressor to beat-wise estimates, we used the value from raw timeseries closest to the time of each R-
 254 peaks. We added the estimated intercept to the residuals from this model as the "residualized"
 255 contractility timeseries, i.e., with the effects of the above three regressors removed. Given both
 256 between-subject and within-subject variation in heart rate, we next applied temporal resampling of each
 257 block's residualized timeseries to allow meaningful comparisons across participants. For this, we used
 258 one-dimensional linear interpolation across time to recreate residualized timeseries sampled at equal
 259 time intervals. Specifically, we took 479 estimates, spaced exactly one second apart, from 2 seconds
 260 post block onset until 480 seconds post block onset (interpolated contractility timeseries). Finally, these
 261 interpolated contractility timeseries were normalized as a t-statistic, i.e., each interpolated contractility
 262 estimate expressed as a t-statistic relative to the timeseries's remaining 478 values. We refer to this t-
 263 statistic-normalized timeseries from now on as the "contractility" timeseries. A grand average
 264 contractility timeseries across participants, separately for each block, is presented in Figure 4.

265



266

267 Figure 4: Grand average time series of contractility across participants for left and right hand blocks of trials.

268 *Bayesian modeling framework*

269 The primary objective of this analyses was to determine whether TREV could reliably capture

270 increases in group-level contractility that corresponded to the events in the grip task, either in response

271 to, or in anticipation of a grip. For this, we used a hierarchical Bayesian framework which hypothesized

272 that the ($n=30$) group distribution of contractility estimates at each timepoint (t) formed a Student's T
273 distribution, $T(t) \sim \text{Student's } T(\mu(t), \text{sig}(t), \nu)$. We formally considered contractility to have increased
274 beyond baseline at a given moment where the estimated mean of a timepoint's distribution ($\mu(t)$)
275 credibly exceeded the mean across all timepoints (M_{μ}). M_{μ} is itself fitted in the same model as the
276 mean of a hierarchical Gaussian distribution (G_{μ}) which constrains estimates of each $\mu(t)$ by serving as
277 their prior ($G_{\mu} \sim N(M_{\mu}, S_{\mu})$). Given how Bayes theorem ascribes joint probabilities to both the prior and
278 the observed data in posterior estimates, this distributional hierarchical framework is inherently
279 conservative with respect to type one error for each estimate of $\mu(t)$. For example, if most values for
280 $\mu(t)$ are within a tight range (as we would expect in a dataset of contractility values with long rest
281 periods between grips), the hierarchical distribution will be characterized by a more certain mean and
282 low variance (low value of S_{μ}), which would then serve as a strict prior on $\mu(t)$ estimates, biasing them
283 toward the group mean (i.e., a nail that stands out gets hammered in). This hierarchical framework
284 therefore requires strong evidence before any $\mu(t)$ is formally accepted as a credible departure. In
285 other words, in a context requiring multiple hypothesis tests, the hierarchical Bayesian framework
286 imposes an adjustment to the level of evidence needed for credible effects, where the data itself
287 determines that level of adjustment instead of an arbitrary criterion (e.g., Bonferroni).

288 We fitted a hierarchical model separately for blocks where grip was administered with the right
289 and left hand. In each case, the specific free parameters of our model were: $\mu(t)$ and $\sigma(t)$, i.e., the
290 479 timepoint-specific mean and standard deviation parameters for group-level SNS distributions at
291 each timepoint across each block. We did not fit the ν parameter hierarchically and assigned it the
292 same uninformed prior ($\nu=1$) in each model. As mentioned above, each $\mu(t)$ parameter was
293 constrained by a hierarchical Gaussian distribution (G_{μ}) with free parameters M_{μ} and S_{μ} corresponding
294 respectively to its mean and standard deviation. M_{μ} was assigned an uninformed Gaussian prior, $N(0,1)$,
295 while S_{μ} was assigned an uninformed half-Gaussian prior (forcing values to be positive), $\text{half}N(1)$. Each

296 $\sigma(t)$ was also constrained by hierarchical Gaussian distribution (G_{σ}), which respectively used an
297 uninformed Gaussian and half-Gaussian prior for its two free parameters, i.e., its mean ($M_{\sigma} \sim N(0,1)$)
298 and standard deviation ($S_{\sigma} \sim \text{half}N(1)$). We formally compared each $\mu(t)$ posterior with that of the
299 M_{μ} by computing the minimum-width Bayesian credible interval (Highest Density Interval (HDI)) of $\mu(t)$
300 - M_{μ} and only considered strong evidence of a departure at each timepoint, i.e., where resulting HDIs
301 did not contain zero.

302 Contractility timeseries were z-score normalized prior to fitting across all participants. Each
303 model's posterior distributions were sampled across four chains of 5000 samples (20000 total), after
304 burning an initial 5000 samples per chain to tune the sampler's step-size to reach 0.95 acceptance. We
305 estimated HDIs using the default setting in the arviz package (Kumar, Carroll, Hartikainen, & Martin,
306 2019).

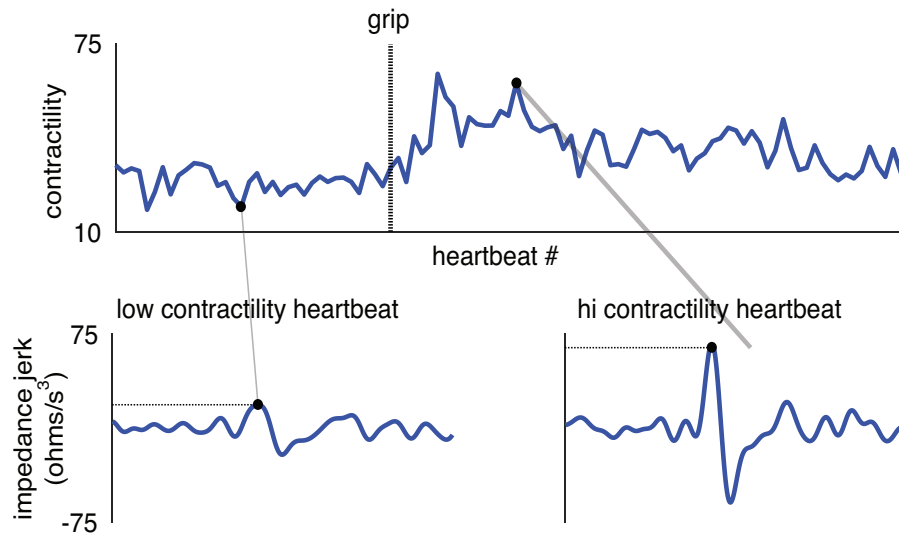
307 *Sliding window rate of change*

308
309 We performed a sliding window deterministic regression to enumerate the rate of change in
310 contractility at each point in our timeseries. At each timepoint we estimated the rate of change in
311 contractility over the ensuing 20 seconds of the timeseries. Specifically, for each timepoint (t) we fitted a
312 distribution of coefficients ($B(t)$), containing five thousand coefficients ($b(k)$), where each $b(k)$ estimated
313 the relation between an arbitrary time vector $[1, \dots, 20]$ and independent draws from the proceeding 20
314 posteriors of μ , i.e., the 20-element vector $[[\mu(t)](k), \dots, [\mu(t+19)](k)]$. To identify credibly positive
315 rates of change, we tested whether 97% of each deterministic distribution ($B(t)$) was above zero.

316 Results

317 We tested whether a thorax-independent monitor of cardiac impedance (TREV) could reliably
318 describe fluctuations in cardiac contractility that credibly exceed baseline as human participants perform
319 a task known to drive increased cardiovascular sympathetic stress. Thirty participants completed both
320 blocks of three incentivized max-intensity grips, with rest periods of two minutes both between each grip

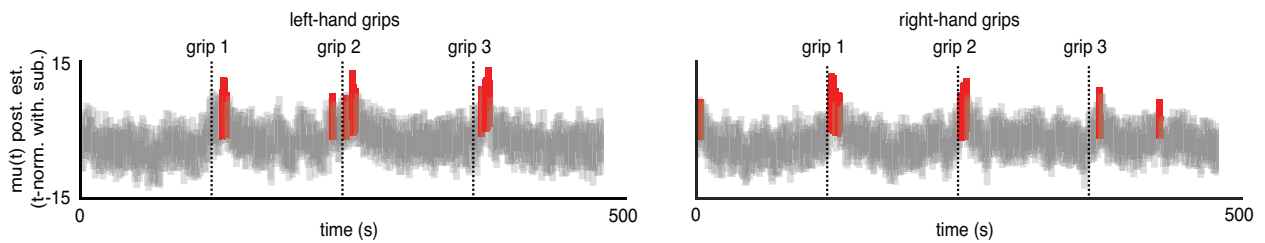
321 and following the final grip. Participants showed strong motivation to grip at maximum intensity,
 322 supported by 29 out of 30 achieving a bonus payment (contingent on beating their predetermined max
 323 threshold) with at least one hand, and 21 out of 30 achieving the bonus payment with both. Figure 5
 324 depicts exemplar contractility for two heartbeats from a single subject, one in the rest phase prior to the
 325 second grip with their right hand and another in the grip's immediate aftermath.



326
 327 Figure 5: Top row is a sample timeseries of contractility estimated at 100 heartbeats. Bottom row shows how
 328 contractility is estimated from impedance jerk timeseries at two single heartbeats.
 329

330 After linear resampling to temporally align contractility across participants and normalizing each
 331 block separately as a t-statistic, group-level contractility in temporal approximation to each grip was
 332 assessed. The results of the hierarchical Bayesian model fitted to contractility timeseries accompanying
 333 left-hand grips are depicted in the left panel of Figure 6. TREV reliably captured contractility exceeding
 334 baseline following grips with the left hand. Left hand grips were accompanied by credible baseline
 335 departure in seconds after grip onset at grip 1: [11, 12, 13, 15], grip 2: [-8, 5, 10, 11, 13] and grip 3: [8,
 336 12, 13, 14, 15]. Each grip was therefore accompanied by at least 4 individual seconds of credible
 337 baseline departure. Departures mostly followed the grips and never followed a grip by more than 15

338 seconds. Each grip was associated with at least two consecutive seconds of baseline departure, with grip
339 3 associated with the longest sustained peak contractility (four consecutive points).



340

341 Figure 6. Results of hierarchical Bayesian model depicting credible departures from baseline contractility (in red) for
342 left and right hand grips.

343

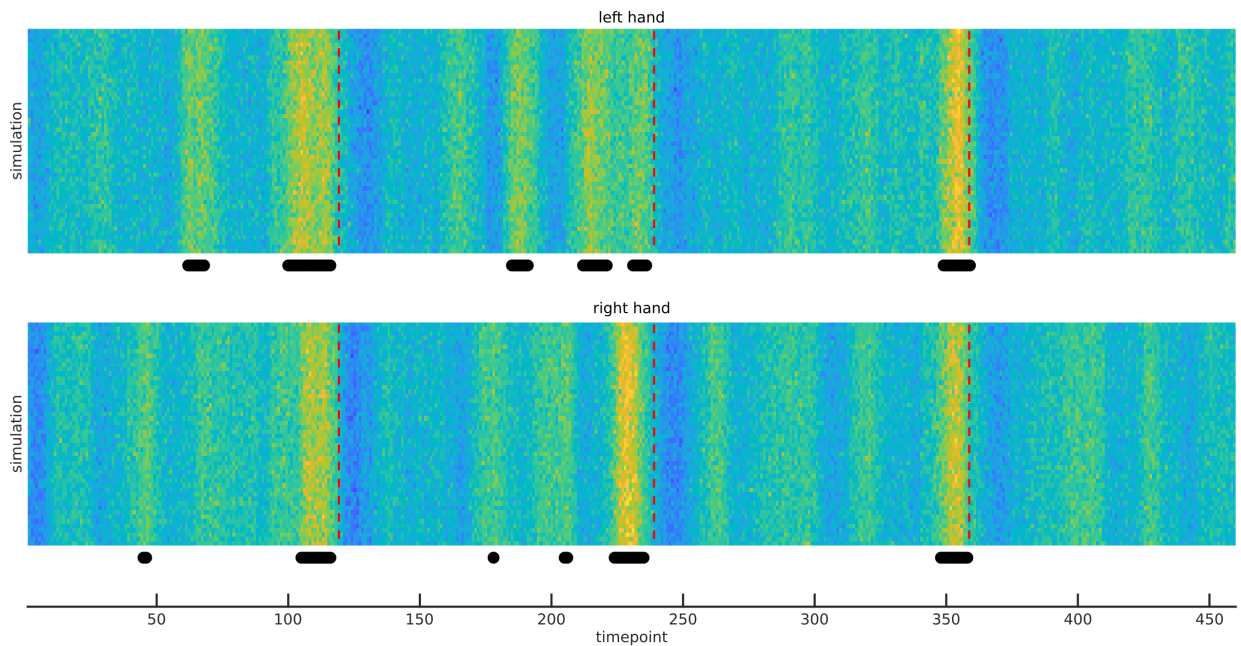
344 The results of the hierarchical Bayesian model fitted to contractility timeseries accompanying
345 right-hand grips are depicted in the right panel of Figure 6. Right-hand grips were accompanied by
346 credible baseline departure after grip onset (in seconds) for grip 1: [-114, 5, 6, 7, 8, 9, 12, 13], grip 2: [4,
347 5, 6, 7, 8, 9] and grip 3: [11, 66]. Discounting the two outliers (preceding grip 1 and following grip 3),
348 each grip was therefore accompanied by at least 1 second of credible baseline departure. Departures all
349 followed the grips and never followed a grip by more than 13 seconds. Grip 2 was associated with the
350 longest sustained peak contractility (six consecutive points). TREV again appeared to reliably capture
351 contractility exceeding baseline following grips with the right hand, although a pair of outliers were
352 present and the duration of peak contractility seemed to abate over the course of the three grips.

353 *Sliding window rate of change*

354

355 As depicted in Figure 7, for both the left and right-hand grips, the rate of change was credibly
356 positive at numerous timepoints in the series preceding each grip. For the left hand, the earliest of these
357 credible pre-grip changes occurred at $t=62$, i.e., 58 seconds prior to the first grip; at $t=185$, i.e., 55
358 seconds prior to the second grip; and at $t=349$, i.e., 11 seconds prior to the third grip. For the right
359 hand, the earliest of these credible pre-grip changes occurred at $t=45$, i.e., 75 seconds prior to the first
360 grip; at $t=178$, i.e., 62 seconds prior to the second grip; and at $t=348$, i.e., 12 seconds prior to the third

361 grip. Interestingly, therefore, we observed a trend in both hands, whereby the rate of change became
362 credibly positive much closer to the initiation of the grip by the third grip, consistent with the allostatic
363 principle of participants learning task requirements and reserving a potentially expensive increase in
364 cardiac contractility until the time it was most critically needed.



365
366 Figure 7. Sliding window rate-of-change. Each column of raster plots are 50 samples from distributions of regression
367 coefficients measuring change in contractility over next 20-second window. Yellow colors are positive (increasing
368 contractility). Markers below each panel reflect timepoints when 97% of distribution is positive, i.e., credibly positive
369 increase in contractility.

370

371 Discussion

372 There is expanding interest across multiple human research disciplines in robustly capturing
373 event-related perturbations of the sympathetic stress response. Consequently, there a need for new
374 assays of cardiac contractility that both reduce preparatory requirements and offer increased signal
375 strength in the face of background noise. In this study we used a novel trans-radial electrical
376 bioimpedance velocimetry device (TREV), attached to the forearm of human participants, and
377 investigated whether it could reliably capture changes in group-level contractility that corresponded to
378 events known to increase sympathetic drive, a max grip task (Grip Task). We observed that TREV

379 electrodes can be applied relatively quickly with minimal training and preparation, and can even be
380 repositioned (from one arm to the other) efficiently between blocks of a task. We further observed TREV
381 to register easy, visually identifiable beat-to-beat signals from the radial and ulnar artery corresponding
382 to the third derivative of the measured impedance wave. In preprocessing, we could readily control for
383 potential confounding effects of respiratory activity and heart rate on beat-wise contractility timeseries.
384 Then, using a hierarchical Bayesian framework, we observed these contractility timeseries to reliably
385 depart baseline at key events in the Grip Task. Remarkably, these departures were seen at the single-trial
386 level across participants (i.e., without averaging across trials). We therefore conclude that TREV offers an
387 exciting development in cardiac autonomic stress research for human researchers interested in event-
388 related capture of cardiac contractility.

389 We employed a data-driven analysis framework, which used the entire timeseries of data
390 recorded across sessions, to determine when contractility estimated by TREV credibly exceeded baseline
391 fluctuations. The primary advantage of this framework is that it removed all need to impose arbitrary
392 criteria on grip events or contractility activity, i.e., a priori deciding epochs around task events to refine
393 analysis, or a priori deciding a criterion that constituted “credibly exceeding baseline”. The analysis was
394 not assisted by any averaging across events to reduce signal-to-noise. The hierarchical Bayesian
395 framework also imposed conservativeness with respect to credible departures from baseline across a
396 large number of hypothesis tests. We nonetheless revealed reliable group-level increases in contractility
397 at each of the six grips executed by participants. A significant sympathetic response to the physical
398 challenge imposed by the grip task is consistent with motivational intensity theory. This theory posits
399 that the sympathetic response should scale with the level of task difficulty, an effect which has been
400 observed in both cognitive and grip tasks (see: Richter, Gendolla, & Wright, 2016, for a review).

401 Note that our criterion for baseline was the average value across all datapoints in the timeseries,
402 which theoretically incorporates all preparatory increases in sympathetic activity leading up to grip

403 execution. When we employed a slope-based analysis strategy, we additionally observed credible
404 anticipatory changes of contractility just prior to grip onset for all trials and with either hand. This
405 observation is consistent with the role of the sympathetic nervous system in allostatic regulation,
406 providing just enough input and just in time (McEwen & Wingfield, 2003).

407 In conclusion, we observed that thorax-independent TREV reliably captures contractility
408 increases to individual events and offers considerable advantages for capturing event-related cardiac
409 responses in more generalized real-world task settings. Such capture of contractility signals has the
410 potential to greatly contribute toward improving our knowledge of how humans synchronize sympathetic
411 state while monitoring broader state information, allowing us to develop more holistic technologies for
412 human-machine integration that can assist with situational awareness, maneuverability and decision
413 making.

414

415 III. Jupyter based signal processing software

416 In the following section, we describe public domain signal processing software operable on any
417 Unix based system (Mac OS, Linux) and a tutorial for streamlining the conversion of TREV impedance
418 measurements into beat-by-beat estimates of contractility. The software, SCOT: Semi-automated
419 Contractility estimates from Ohmic impedance measured with TREV, uses the Jupyter Notebook and is
420 downloadable at <https://github.com/caitgregory/SCOT>. Unless otherwise specified, the pipeline uses
421 the Tkinter package to manage all GUI interactions and Matplotlib (Hunter, 2007) to manage plots. It is
422 currently configured to interact with output files from AcqKnowledge (BIOPAC); however, it theoretically
423 could be amended to work with other file formats. Users can fully test or replicate this pipeline by
424 downloading an example data set from the tutorial at
425 <https://github.com/caitgregory/SCOT/blob/main/tutorial.md>. The example data were recorded for 45
426 minutes during a simultaneous fMRI recording while human participants performed speeded reaches

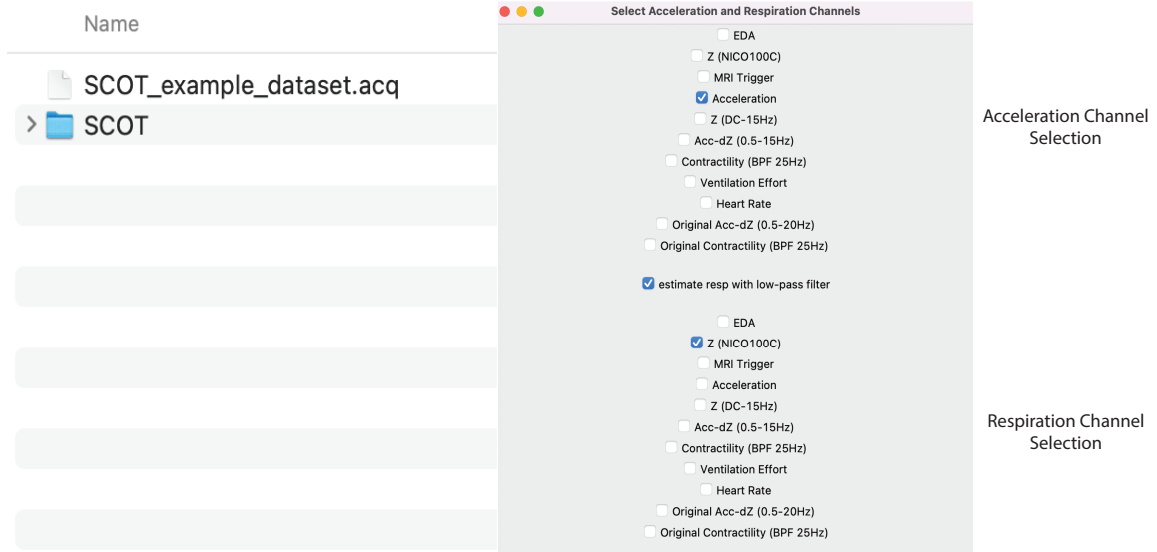
427 with a joystick. These data were minimally preprocessed during acquisition using AcqKnowledge
428 Software by performing an online lowpass filter (max cutoff = 20 Hz) and the calculation of stroke
429 acceleration, dZ/dt .

430 *Pipeline Processing*

431 In four largely automated steps, users are able to import the data (Jupyter Notebook, Cell 1),
432 identify beat by beat time intervals (Cells 2 and 3), estimate cardiac contractility at each beat (Cell 4), and
433 remove artifacts related to heart rate and respiratory activity (Cell 5).

434 Cell 1 of the Jupyter Notebook loads the data via a GUI (Figure 8) using the bioread functions
435 (Vack, 2023). (To replicate the pipeline, users can use the AcqKnowledge file IV_301_1.acq). The
436 resulting menu allows users to specify the appropriate acceleration channel and respiration channels
437 defined during the acquisition. Note that the pipeline imports the stroke acceleration channel (which
438 provides more easily identifiable peaks relative to noise. Here, users can also specify if the acceleration
439 channel or the respiration channel require a FIR low-pass filter. We have preset the cutoff of these filters
440 in the notebook at 22.5 Hz and 0.35 Hz, respectively. The filters use a Hamming window and a length
441 computed by the convention used in freely available packages for processing electrophysiological data
442 (MNE; (Gramfort, et al., 2013). Specifically, we construct a filter using the firwin function (SciPy; (Virtanen,
443 et al., 2020) with a length of N . N is computed with $3.3 \times 1/tb$. Here, tb is a transition bandwidth which is
444 the minimum value between $f1$ and $f2$, where $f1$ is the maximum between one quarter of the specified
445 cutoff and 2, and $f2$ is the Nyquist frequency minus the specified cutoff. We then apply the filter using
446 the lfilter function (SciPy) and adjust the phase shift by discarding the first $N/2$ samples of data and
447 readjusting the time points. The user exits out of the menu which initiates the above steps. Depending
448 on the length of the data this initial import could take a couple of minutes. A notice will appear in the
449 cell output once this step is complete.

450



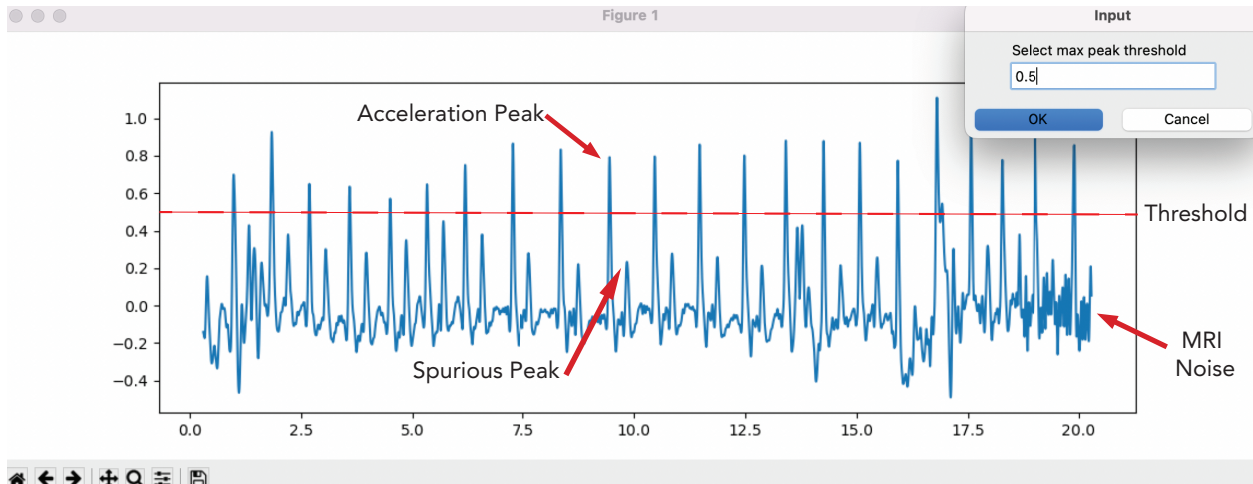
451

452 Figure 8: Cell 1 GUI.

453

454 Cells 2 and 3 identify the time interval between each heartbeat by finding peaks in the
455 acceleration timeseries. As noted above, the acceleration timeseries (dZ/dt) is more robust to noise than
456 the contractility timeseries (d^2Z/dt^2), allowing for an easier identification of peaks. The program uses the
457 SciPy findpeaks function which we preset to find peaks spaced at least 0.5 seconds apart (equivalent to a
458 heart rate of 120 BPM). In Cell 2, (Figure 9) users can visually inspect a 20 second portion of the
459 acceleration timeseries at time to identify a minimum threshold for peak amplitude, which they manually
460 input. In addition to the minimum spacing, this peak amplitude threshold acts as an extra automated
461 control against spurious peak identification. On the sample data set, we selected a minimum threshold
462 value of 0.5.

463



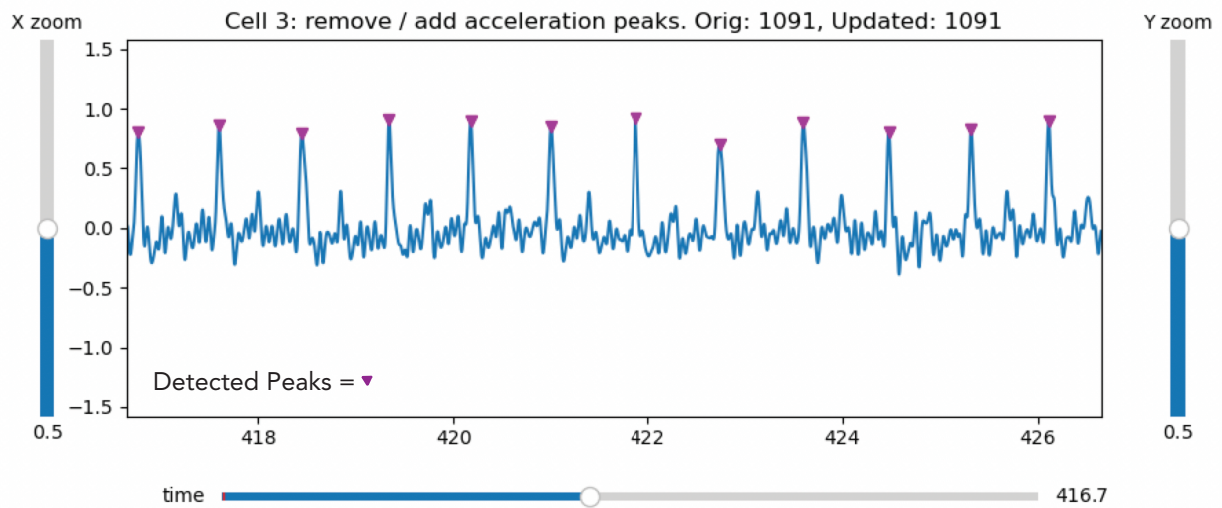
464

465 Figure 9: GUI for cell 2. Note the peak threshold is inputted as 0.5. This threshold value helps avoid flutter between
 466 acceleration peaks. The participant has a premature ventricular contraction at time 16.5s (causing a reduction of
 467 contractility due to reduced ventricular filling). Also note the onset of MRI scanning at 18 seconds. Despite the
 468 associated MRI associated noise, acceleration peaks are still visible and robust.
 469

470 Cell 3 (Figure 10) allows users to manually add and remove heart beats via an interactive
 471 timeseries of the acceleration waveform. Users can scroll through the data and identify any peaks that
 472 the program may have missed or mis-labeled. There are three keyboard options that allow the user to
 473 edit the pre-determined time points of the peaks. Using a two-button mouse, or equivalent keystrokes
 474 and clicks for a one-button mouse, a left click will add a peak and a right click will remove a peak. If is
 475 there is noise in the signal at any point or the user is unsure where exactly the peak should go, the user
 476 can press m + left click. Here, the script performs a moving ensemble average of the two previous and
 477 two consecutive peaks to determine the location of the peak of interest.

478

479

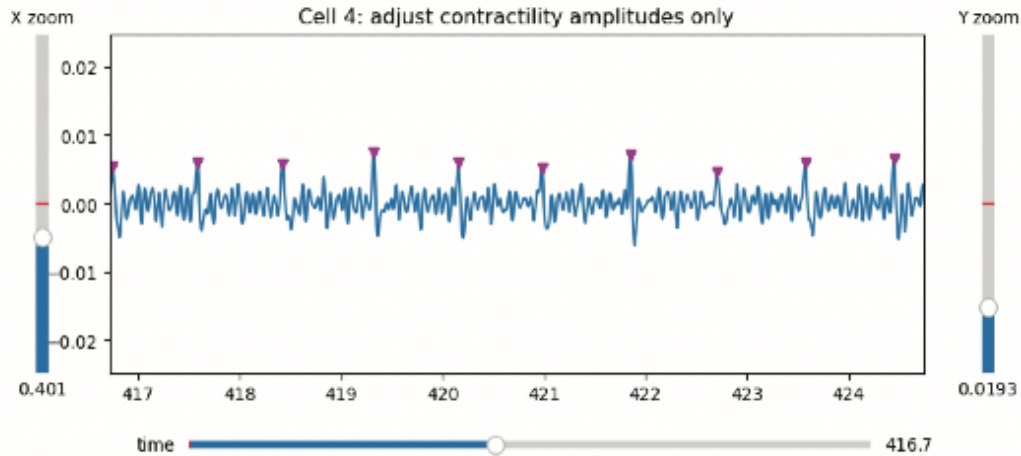


480

481 Figure 10: Cell 3 GUI. The acceleration time series plotted over time with detected peaks. The user is
 482 able to use the slider along the bottom of the graph to scroll through the data and adjust the peak
 483 location as needed.

484

485 Cell 4 (Figure 11) plots the contractility timeseries (the derivative of acceleration). Note that in
 486 cell 3 we found the maximum values of the acceleration timeseries, i.e., the critical values such that
 487 $d^2Z/dt^2 = 0$. Given that maximum acceleration is reached after peak contractility, the time points of
 488 peaks identified in cells 2 and 3 need to be adjusted backward in time. We accordingly search for
 489 maximum contractility amplitude in the time window spanning 250 ms prior to the identified acceleration
 490 peak. Users can scroll through the data and manually adjust the identified peak amplitude if necessary.
 491 Note that in this cell we are interested in peak contractility amplitude values rather than time points.



492

493 Figure 11: Cell 4 GUI. The contractility timeseries plotted over time.

494

495 Lastly, Cell 5 removes the influence of heart rate and respiration from the contractility estimates
 496 using the residualizing method described in the methods section above. Briefly, a multiple regression
 497 was conducted where contractility is modeled as a function of the heart rate, respiratory amount, and
 498 respiratory cycle at each heartbeat. Heart rate is computed from the inter-beat intervals identified in cell
 499 3. Respiratory amount and cycle are identified by first finding each consecutive cosine-like segment in
 500 the specified respiration timeseries. Y-axis values (i.e. respiration amount) of each segment are
 501 demeaned while x-axis values (i.e., respiration phase) are normalized between 0 and 2π . We then extract
 502 the respiratory amount and phase values closest to each heartbeat. Prior to the regression, each
 503 regressor is z-scored. We output the residuals of the regression model as the contractility estimates with
 504 the effects of heart rate and respiration removed. Once completed, data are outputted into a csv file
 505 with each row corresponding to a heartbeat, and columns with the time of each heartbeat (relative to the
 506 beginning of the recording) and the contractility amplitude. By default, the csv will be named the same
 507 as the input AcqKnowledge file with the csv extension; however, users can change this through a GUI.

508

509 Acknowledgements

510 Supported by the Institute for Collaborative Biotechnologies under Cooperative Agreement

511 W911NF-19-2-0026, contract W911NF-19-D-0001, and grant W911NF-16-1-0474, all from the Army

512 Research Office. The content of the information does not necessarily reflect the position or the policy of

513 the Government and no official endorsement should be inferred.

514

515

516

517

518

- 520 Bernstein, D.P. (2009). Impedance cardiography: Pulsatile blood flow and the biophysical and
 521 electrodynamic basis for the stroke volume equations. *J Electrical Bioimpedance*, **1**, 2-17.
- 522 Bernstein, D.P., Henry, I.C., Banet, M.J., & Dittrich, T. (2012). Stroke volume obtained by electrical
 523 interrogation of the brachial artery: transbrachial electrical bioimpedance velocimetry.
 524 *Physiological Measurement*, **33**, 629-649.
- 525 Bernstein, D.P., Henry, I.C., Lemmens, H.J., Chaltas, J.L., DeMaria, A.N., Moon, J.B., & Kahn, A.M.
 526 (2015). Validation of stroke volume and cardiac output by electrical interrogation of the brachial
 527 artery in normals: assessment of strengths, limitations, and sources of error. *Journal of Clinical*
 528 *Monitoring and Computing*, **29**, 789-800.
- 529 Cieslak, M., Ryan, W.S., Babenko, V., Erro, H., Rathbun, Z.M., Meiring, W., Kelsey, R.M., Blascovich, J., &
 530 Grafton, S.T. (2018). Quantifying rapid changes in cardiovascular state with a moving ensemble
 531 average. *Psychophysiology*, **55**.
- 532 Dundon, N.M., Garrett, N., Babenko, V., Cieslak, M., Daw, N.D., & Grafton, S.T. (2020). Sympathetic
 533 involvement in time-constrained sequential foraging. *Cognitive, affective & behavioral*
 534 *neuroscience*, **20**, 730-745.
- 535 Dundon, N.M., Shapiro, A.D., Babenko, V., Okafor, G.N., & Grafton, S.T. (2021). Ventromedial Prefrontal
 536 Cortex Activity and Sympathetic Allostatics During Value-Based Ambivalence. *Frontiers in*
 537 *behavioral neuroscience*, **15**, 615796.
- 538 Gramfort, A., Luessi, M., Larson, E., Engemann, D., Strohmeier, D., Brodbeck, C., Goj, R., Jas, M.,
 539 Brooks, T., Parkkonen, L., & Hämäläinen, M. (2013). MEG and EEG data analysis with MNE-
 540 Python. *Frontiers in neuroscience*, **7**.
- 541 Hunter, J.D. (2007). Matplotlib: A 2D Graphics Environment. *Computing in Science & Engineering*, **9**, 90-
 542 95.
- 543 Kumar, R., Carroll, C., Hartikainen, A., & Martin, O. (2019). ArviZ a unified library for exploratory analysis
 544 of Bayesian models in Python. *J Open Source Softw*, **4**, 1143.
- 545 McEwen, B.S., & Wingfield, J.C. (2003). The concept of allostasis in biology and biomedicine. *Horm*
 546 *Behav*, **43**, 2-15.
- 547 Miller, J.C., & Horvath, S.M. (1978). Impedance cardiography. *Psychophysiology*, **15**, 80-91.
- 548 Richter, M. (2015). Goal pursuit and energy conservation: energy investment increases with task demand
 549 but does not equal it. *Motivation and Emotion*, **39**, 25-33.
- 550 Richter, M., Gendolla, G.H.E., & Wright, R.A. (2016). Three Decades of Research on Motivational
 551 Intensity Theory: What We Have Learned About Effort and What We Still Don't Know. *Advances*
 552 *in Motivation Science* (Vol. **3**, pp. 149-186): Elsevier.
- 553 Salvatier, J., Wiecki, T.V., & Fonnesbeck, C. (2016). Probabilistic programming in Python using PyMC3.
 554 *PeerJ Computer Science*, **2**, e55.
- 555 Sel, K., Osman, D., & Jafari, R. (2021). Non-Invasive Cardiac and Respiratory Activity Assessment From
 556 Various Human Body Locations Using Bioimpedance. *IEEE Open J Eng Med Biol*, **2**, 210-217.
- 557 Stanek, J., & Richter, M. (2016). Evidence against the primacy of energy conservation: Exerted force in
 558 possible and impossible handgrip tasks. *Motivation Science*, **2**, 49-65.
- 559 Stanek, J.C., & Richter, M. (2021). Energy investment and motivation: The additive impact of task
 560 demand and reward value on exerted force in hand grip tasks. *Motivation and Emotion*, **45**, 131-
 561 145.
- 562 Vack, N. (2023). bioread 3.0.1. Python Package Index. <https://pypi.org/project/bioread>.
- 563 Virtanen, P., Gommers, R., Oliphant, T.E., Haberland, M., Reddy, T., Cournapeau, D., Burovski, E.,
 564 Peterson, P., Weckesser, W., Bright, J., van der Walt, S.J., Brett, M., Wilson, J., Millman, K.J.,

565 Mayorov, N., Nelson, A.R.J., Jones, E., Kern, R., Larson, E., Carey, C.J., Polat, İ., Feng, Y.,
566 Moore, E.W., VanderPlas, J., Laxalde, D., Perktold, J., Cimrman, R., Henriksen, I., Quintero, E.A.,
567 Harris, C.R., Archibald, A.M., Ribeiro, A.H., Pedregosa, F., van Mulbregt, P., Vijaykumar, A.,
568 Bardelli, A.P., Rothberg, A., Hilboll, A., Kloeckner, A., Scopatz, A., Lee, A., Rokem, A., Woods,
569 C.N., Fulton, C., Masson, C., Häggström, C., Fitzgerald, C., Nicholson, D.A., Hagen, D.R.,
570 Pasechnik, D.V., Olivetti, E., Martin, E., Wieser, E., Silva, F., Lenders, F., Wilhelm, F., Young, G.,
571 Price, G.A., Ingold, G.-L., Allen, G.E., Lee, G.R., Audren, H., Probst, I., Dietrich, J.P., Silterra, J.,
572 Webber, J.T., Slavič, J., Nothman, J., Buchner, J., Kulick, J., Schönberger, J.L., de Miranda
573 Cardoso, J.V., Reimer, J., Harrington, J., Rodríguez, J.L.C., Nunez-Iglesias, J., Kuczynski, J., Tritz,
574 K., Thoma, M., Newville, M., Kümmerer, M., Bolingbroke, M., Tartre, M., Pak, M., Smith, N.J.,
575 Nowaczyk, N., Shebanov, N., Pavlyk, O., Brodtkorb, P.A., Lee, P., McGibbon, R.T., Feldbauer, R.,
576 Lewis, S., Tygier, S., Sievert, S., Vigna, S., Peterson, S., More, S., Pudlik, T., Oshima, T. (2020).
577 SciPy 1.0: fundamental algorithms for scientific computing in Python. *Nature methods*, **17**, 261-
578 272.
579